



# Dilated cardiomyopathy–associated skeletal muscle actin (ACTA1) mutation R256H disrupts actin structure and function and causes cardiomyocyte hypocontractility

Ankit Garg<sup>a,b,c</sup>, Silvia Jansen<sup>d</sup> , Lina Greenberg<sup>b</sup>, Rui Zhang<sup>b</sup>, Kory J. Lavine<sup>c,e</sup>, and Michael J. Greenberg<sup>b,1</sup>

Edited by Kathleen M. Trybus, University of Vermont, Burlington, VT; received March 10, 2024; accepted September 17, 2024 by Editorial Board Member Yale E. Goldman

Skeletal muscle actin (ACTA1) mutations are a prevalent cause of skeletal myopathies consistent with ACTA1's high expression in skeletal muscle. Rare *de novo* mutations in ACTA1 associated with combined cardiac and skeletal myopathies have been reported, but ACTA1 represents only ~20% of the total actin pool in cardiomyocytes, making its role in cardiomyopathy controversial. Here we demonstrate how a mutation in an actin isoform expressed at low levels in cardiomyocytes can cause cardiomyopathy by focusing on a unique ACTA1 variant, R256H. We previously identified this variant in a family with dilated cardiomyopathy, who had reduced systolic function without clinical skeletal myopathy. Using a battery of multiscale biophysical tools, we show that R256H has potent effects on ACTA1 function at the molecular scale and in human cardiomyocytes. Importantly, we demonstrate that R256H acts in a dominant manner, where the incorporation of small amounts of mutant protein into thin filaments is sufficient to disrupt molecular contractility, and that this effect is dependent on the presence of troponin and tropomyosin. To understand the structural basis of this change in regulation, we resolved a structure of R256H filaments using cryoelectron microscopy, and we see alterations in actin's structure that have the potential to disrupt interactions with tropomyosin. Finally, we show that *ACTA1*<sup>R256H/+</sup> human-induced pluripotent stem cell cardiomyocytes demonstrate reduced contractility and sarcomeric organization. Taken together, we demonstrate that R256H has multiple effects on ACTA1 function that are sufficient to cause reduced contractility and establish a likely causative relationship between ACTA1 R256H and clinical cardiomyopathy.

actin | cardiomyopathy | contractility | muscle

Dilated cardiomyopathy (DCM) is a leading cause of heart failure and left ventricular assist device/cardiac transplantation (1). DCM can be both secondary to another pathologic process, but it also has numerous genetic causes, including mutations in sarcomeric proteins (2). DCM mutations associated with sarcomeric proteins have poorer outcomes to guideline-directed interventions (3) which suggests mechanistic differences in the pathogenesis of these patients' DCM. As our appreciation for the mechanistic heterogeneity of DCM grows, it becomes imperative to utilize multiscale analysis to study unique phenotypes so we may better utilize available therapies and identify new targets (4).

While some genes have been unambiguously associated with DCM including cardiac myosin and titin, there is ambiguity about the roles of other genes in DCM pathogenesis (5). In part, this ambiguity stems from the small number of patients with these mutations and a lack of understanding of the connections between variants and the disease phenotype. One such gene with a controversial role in DCM is skeletal muscle actin, ACTA1. Actin is one of the most conserved and highly expressed proteins in eukaryotes. Six isoforms of actin are expressed in humans, and two isoforms, ACTA1 and ACTC1 (referred to as "cardiac actin"), are specific to sarcomeres (6). Actin is a principal component of the sarcomere thin filament, where it binds to troponin and tropomyosin, which regulate the calcium-dependent interactions between myosin and the thin filament (4). Mutations perturbing contraction can cause skeletal myopathies and cardiomyopathies (7). ACTA1 is expressed at high levels in skeletal muscle and an order of magnitude less in cardiac muscle where ACTC1 expression dominates (6). Given this specificity, multiple mutations in ACTA1 have been associated with skeletal myopathies while ACTC1 mutations have been associated with cardiomyopathies. With the low expression of ACTA1 in the heart and high expression in skeletal muscle, some have speculated that ACTA1 mutations would have no impact on cardiac contractility (8); however, rare cases of DCM with combined skeletal myopathy have since been identified in patients bearing ACTA1

## Significance

Skeletal muscle actin mutations are well known to cause skeletal myopathies, but their role in cardiomyopathies has been controversial as skeletal muscle actin is only expressed at modest levels in the heart. Here, we demonstrate that a skeletal muscle actin mutation potentially causes multiple defects in actin function at the atomic and molecular scales, and it functions in a dominant fashion, leading to cardiomyocyte contractile defects. Our results establish how skeletal muscle actin mutations may cause cardiomyocyte dysfunction and lay the foundation for future studies of the role of skeletal muscle actin in cardiomyopathy.

Author affiliations: <sup>a</sup>Division of Cardiology, Department of Medicine, Johns Hopkins University, Baltimore, MD 21205; <sup>b</sup>Department of Biochemistry and Molecular Biophysics, Washington University School of Medicine, St. Louis, MO 63110; <sup>c</sup>Cardiovascular Division, Department of Medicine, Washington University School of Medicine, St. Louis, MO 63110; <sup>d</sup>Department of Cell Biology and Physiology, Washington University in St. Louis, St. Louis, MO 63110; and <sup>e</sup>Department of Pathology and Immunology, Washington University School of Medicine, St. Louis, MO 63110

Author contributions: A.G., S.J., L.G., R.Z., K.J.L., and M.J.G. designed research; A.G. and L.G. performed research; A.G. contributed new reagents/analytic tools; A.G., L.G., and R.Z. analyzed data; and A.G., S.J., R.Z., K.J.L., and M.J.G. wrote the paper.

The authors declare no competing interest.

This article is a PNAS Direct Submission K.M.T. is a guest editor invited by the Editorial Board.

Copyright © 2024 the Author(s). Published by PNAS. This article is distributed under [Creative Commons Attribution-NonCommercial-NoDerivatives License 4.0 \(CC BY-NC-ND\)](https://creativecommons.org/licenses/by-nc-nd/4.0/).

<sup>1</sup>To whom correspondence may be addressed. Email: greenberg@wustl.edu.

This article contains supporting information online at <https://www.pnas.org/lookup/suppl/doi:10.1073/pnas.2405020121/-DCSupplemental>.

Published November 6, 2024.

mutations (9–12). To date, no studies have established cardiac pathogenicity of these ACTA1 mutations nor the underlying mechanism.

We previously described the unique R256H (also referred to as R254H when using the posttranslationally cleaved actin numbering convention; henceforth referred to as “postcleavage” numbering) variant in ACTA1 which was associated with DCM in *ACTA1*<sup>R256H/+</sup> patients but uniquely lacked a clinical skeletal myopathy typically seen with ACTA1 mutants (13). Unlike previous ACTA1-associated DCM mutations which were de novo mutations affecting single patients, this report demonstrated an ACTA1 DCM variant in multiple patients within a family. There was a subsequent report of a similar ACTA1 variant, G253S, that also appeared to be associated with DCM without skeletal myopathy (14). Though these variants provided evidence for ACTA1 having a role in cardiomyopathy, it was unknown how a low expressed actin isoform in the heart could affect cardiac contractility.

Here, we used multiscale computational and experimental tools spanning from atoms to cells to understand the mechanism of the ACTA1 R256H variant. Our results demonstrate that R256H perturbs multiple actin functions, including a potent effect on contractility, and they provide insights into how mutations in the skeletal muscle actin isoform can cause cardiomyopathy.

## Results

**Molecular Dynamics Simulations Show That R256H Alters the Structural Dynamics of Monomeric ACTA1.** To gain insights into the atomic-level changes induced by the R256H variant, we used molecular dynamics (MD) simulations. The structure of the ACTA1 monomer has been extensively modeled (15) and used in molecular dynamics simulations (16). For our starting structure, we utilized the monomeric structure of ACTA1 bound to adenosine diphosphate (ADP) and calcium (PDB 1J6Z) (17). All our simulations were performed in explicit water. We ran five separate 1  $\mu$ s simulations for the WT ACTA1. For the R256H mutant, a histidine was introduced into the structure, and at physiological pH, His residues can exist in 3 separate states: “HSD” neutrally N $\delta$  protonated, “HSE” neutrally N $\epsilon$  protonated, and “HSP” doubly protonated His. Therefore, we also ran five separate 1  $\mu$ s simulations for each of these possibilities (R256HSD, R256HSE, and R256HSP).

To quantify the differences between structures, we calculated the RMS displacement (RMSD) of the structures relative to the average WT structure. The RMSDs for each protonation state of the mutant were significantly different from WT ACTA1 (*SI Appendix, Fig. S1 A and B*), demonstrating that the mutation affects the mean structure of ACTA1, regardless of the protonation state. To better understand where these changes might arise, we calculated the RMSD per residue compared to the average WT structure. Residues with the greatest change in RMSD appeared to concentrate in subdomains 2 and 4 (*SI Appendix, Fig. S1 C*), suggesting that R256H induces allosteric changes that affects both of these subdomains.

Since subdomains 2 and 4 are close to each other in the nucleotide-bound state, and the mutant shows large changes in the RMSD of these domains, we hypothesized that the mutation could affect nucleotide binding and/or dissociation. While our simulations were not capable of modeling nucleotide binding, they showed the rapid loss of ADP from actin. We found that the time to the loss of bound ADP was significantly faster for the R256HSE and R256HSP ACTA1 compared to WT ACTA1, and R256HSD trended toward faster dissociation (*Fig. 1 A and B*). Taken together, our simulations predict that R256H changes the

structural dynamics of ACTA1, potentially affecting nucleotide binding.

**R256H Reduces Actin Stability and Impairs Actin Polymerization.** To biochemically assess differences between WT and R256H ACTA1, we required R256H ACTA1 protein; however, recombinant ACTA1 has been difficult to purify in sufficient quantities and purity. We adapted an SF9/baculovirus system that has been successfully used to produce other  $\alpha$ -actins including mutant actins (18–21). Previous SF9 ACTA1 purification strategies either overexpressed untagged ACTA1 which could copolymerize with endogenous SF9 actin, resulting in decreased purity, or they utilized a nonpolymerizable tag whose proteolytic cleavage left multiple nonnative amino acids (22). We employed an expression strategy utilizing a chymotrypsin-cleavable C-terminal tag composed of thymosin  $\beta$ 4 (TMSB4) to block polymerization in tandem with a multihistidine tag that has been successfully used to purify functional wildtype and mutant ACTA2 (smooth muscle actin) (23), which is similar to ACTA1 (*SI Appendix, Fig. S2*). We successfully applied this system to generate both WT and R256H ACTA1 recombinant proteins with yields ranging from 0.4 to 0.9 mg per 250 mL of SF9 culture.

Our molecular dynamics simulations predict that R256H affects the structure of the actin monomer, leading to altered nucleotide binding and/or exchange. To test whether the mutation affects nucleotide exchange, we measured the rate of exchange on actin between ADP and the fluorescent reporter  $\epsilon$ ATP. We incubated WT and R256H ACTA1-ADP with  $\epsilon$ ATP, and then we measured the time course of the increase in fluorescence signal upon  $\epsilon$ ATP binding (*Fig. 1 C*). We saw that both tissue-purified skeletal actin and recombinant actin showed similar rates of exchange where the fluorescence change as a function of time is well fitted with a single exponential function (*SI Appendix, Fig. S3A*); however, R256H ACTA1 had a significantly slower nucleotide exchange rate (0.014 s<sup>-1</sup> for WT vs. 0.0013 s<sup>-1</sup> for R256H; *Fig. 1 C*) that was almost linear during the course of the experiment. Due to this, it was not possible to unambiguously distinguish whether the change in the observed rate seen with the mutant was due to altered ADP release and/or adenosine triphosphate (ATP) binding; however, our observations are consistent with the prediction of altered nucleotide binding stability seen in the MD simulations.

It is well established that nucleotide binding is important to G-actin stability and polymerization (24). Therefore, we set out to test the effects of R256H ACTA1 on thermal stability and actin polymerization. To test whether globular (i.e., monomeric) ACTA1 R256H had altered thermal stability, we used a protein thermal shift assay. We found that the melting temperature of R256H ACTA1 (46.1 °C) was significantly lower than the melting temperature of WT ACTA1 (58.9 °C) (*Fig. 2A*), consistent with the observed changes in nucleotide binding.

Next, we measured the kinetics of polymerization using pyrene-labeled actin which shows increased fluorescence when actin is integrated into a filament (25). The time course of spontaneous polymerization has been extensively studied, and follows a typical sigmoidal relationship, consisting of an initial slow growth lag phase whose duration is related to actin nucleation, a rapid linear growth phase largely driven by filament elongation, and then a steady state phase (26). It should be noted that the spontaneous pyrene actin polymerization assays provide measurement of the total amount of polymerized actin at a given time which has a complex dependence on the concentration of free actin, the critical concentration of the actin, the number of available filament free ends, and the rates of monomer addition and loss from filaments. As such, it is not possible to unambiguously

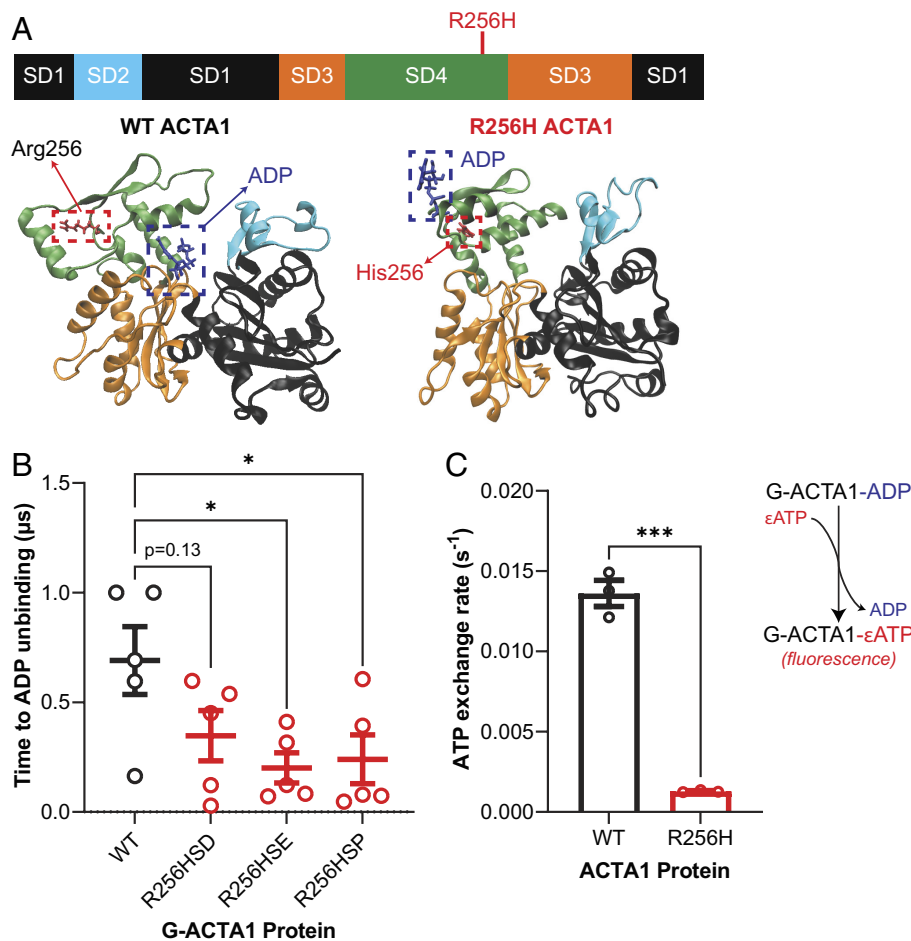


**Fig. 1.** Simulations of G-ACTA1 R256H predict decreased nucleotide binding stability which is corroborated by decreased nucleotide exchange rates. (A) (Top) Cartoon representing the domain architecture of ACTA1 with individual subdomains ("SD") colored to correspond to colors seen throughout the figure. The position of the R256H mutation is indicated in red. (Bottom) Representative single frame captures from molecular dynamics simulations of the ACTA1 1J6Z starting structure in the WT (Left) and R256H mutated (Right) states. Shown in the red dashed box is the 256 residue and in the blue dashed box is the ADP nucleotide. Note the loss of ADP from the binding pocket in R256H. (B) R256H ACTA1 binding time to ADP is shorter than WT ACTA1. Binding time is defined as the amount of time that the ADP molecule lies within 20 Å of the center of mass of ACTA1. Data are obtained from five 1  $\mu$ s simulations. \* $P$  < 0.05 as calculated by ANOVA with multiple comparison testing followed by Dunnett correction. (C) R256H ACTA1 exchanges ATP slower than WT ACTA1. (Top) Outline of ATP exchange assay. Fluorescent signal increases as ADP is displaced and ATP binds to G-ACTA1. (Bottom) ATP exchange rates that were calculated from the slopes of three separate replicates per condition found in *SI Appendix, Fig. S3*. For WT,  $k = 0.014 s^{-1}$  and for R256H  $k = 0.0013 s^{-1}$ . \*\*\* $P$  < 0.001 as calculated by a two-tailed  $t$  test. All error bars represent SEM.

extract rate constants for specific processes (e.g., elongation) from these experiments alone; however, they still provide insights into these processes. Due to the inability to directly discern the second-order elongation rate constant from the observed rates seen in this experiment, we refer to the slope of the linear growth phase as "observed linear growth rate."

Consistent with the expected sigmoidal response curve, WT actin clearly follows this relationship, and the lag phase becomes shorter at higher actin concentrations (Fig. 2B). Compared to WT, R256H ACTA1 demonstrates altered polymerization kinetics. Its lag phase, which is typically a reflection of the nucleation rate, is visually prolonged even at the highest concentrations of R256H actin tested. Moreover, the observed linear growth rate was slower for R256H ACTA1 than WT ACTA1 over all concentrations tested except for 4  $\mu$ M (Fig. 2C, Left graph). With these two effects combined, R256H ACTA1 has an increased time to half-maximum intensity (Fig. 2C, Right graph). However, given the substantial increase in the observed lag phase with R256H ACTA1, and the inherent inability of pyrene-labeled actin polymerization to unambiguously determine the elongation rate, it was not possible to determine whether the second-order elongation rate constant was affected by the mutation.

To directly test how the mutation affects actin filament nucleation and growth, we employed total internal reflection (TIRF) microscopy to visualize growing actin filaments incorporating fluorescent actin monomers in real time. Consistent with the prolonged lag phase and decreased slope of the linear growth phase seen in our pyrene polymerization assay (Fig. 2B), R256H ACTA1 had significantly decreased nucleation and observed filament growth rates at 2  $\mu$ M actin (Fig. 2D). Notably, the visual growth of many R256H ACTA1 filaments showed intermittent growth and disassembly. Averaged over several frames, this appeared as a slowed overall growth rate. However, some filaments had overall disassembly which was observed as negative growth rates (*SI Appendix, Fig. S5D*), and we cannot distinguish whether this is due to halted growth with disassembly overtaking assembly or an overall higher disassembly rate.

The observed filament growth rate by TIRF is the combined effect of simultaneous filament assembly, which depends on the concentration of free actin, and disassembly. The concentration of actin where the assembly rate equals the disassembly rate is known as the critical concentration. A decrease in either the actin-dependent rate of assembly or an increase in the actin-independent disassembly rate would result in an increased

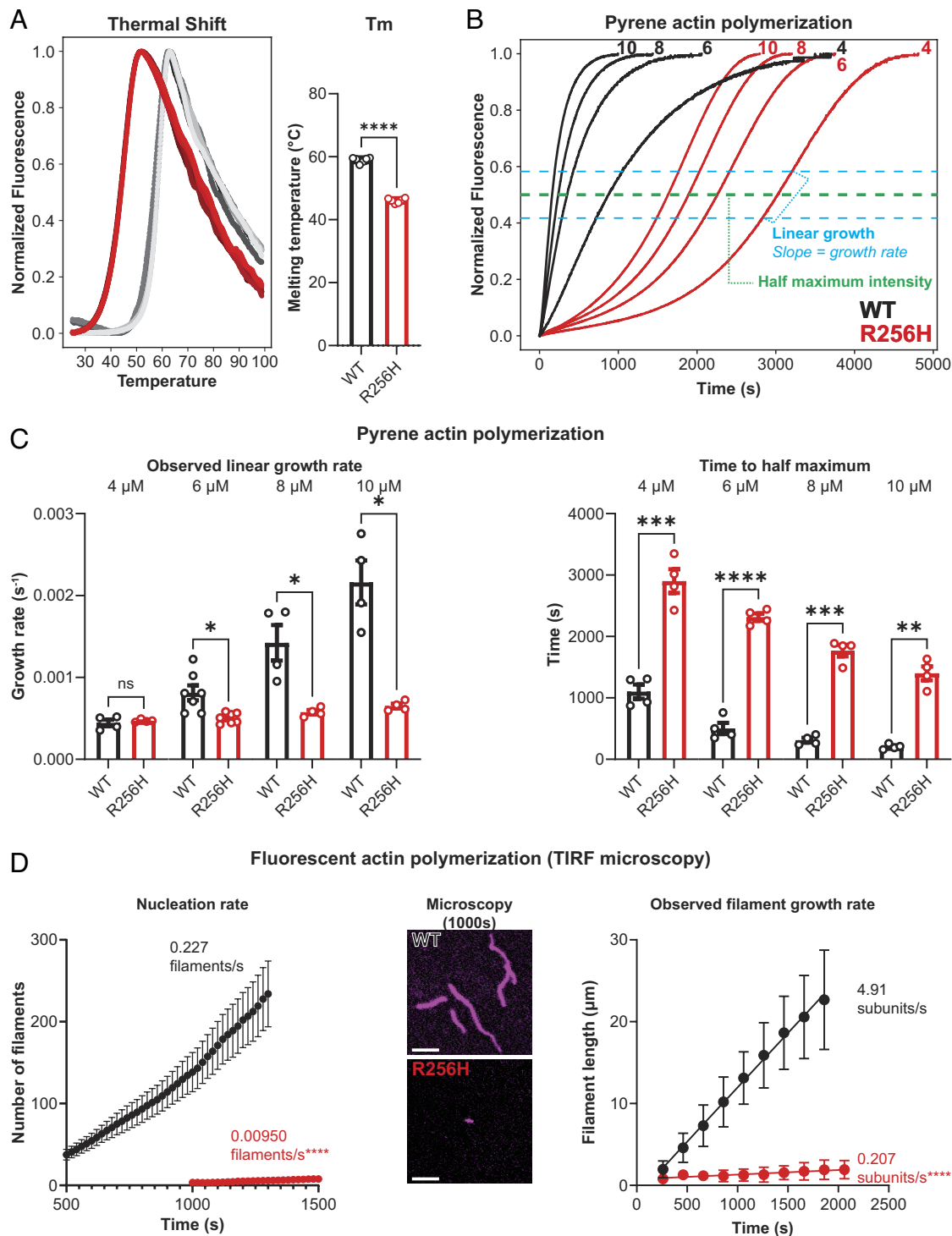


**Fig. 2.** R256H ACTA1 has decreased thermal stability and disrupted polymerization. (A) (Left graph) Normalized fluorescence generated from melting WT and R256H proteins using Thermo Fisher Scientific Protein Thermal Shift™ assay. As protein denatures, the dye binds previously inaccessible hydrophobic regions resulting in increased fluorescence signal. Six traces are present for each sample, but not all six traces are visible due to high similarity between data. (Right graph) Calculated melting temperature. The experiment was performed in triplicate from two independently purified sets of ACTA1 WT and R256H protein ( $n = 6$  for each sample). \*\*\*\* $P < 0.0001$  by the two-tailed  $t$  test. Note that error bars are present but not visible due to small size. (B) Representative traces of pyrene polymerization assays performed at various actin monomer concentrations for WT and R256H ACTA1 (each number above each curve denotes concentration in  $\mu\text{M}$ ). Fluorescence signal increases as actin polymerizes. Note the substantial difference in the kinetics of polymerization between WT and R256H. These are quantified in the proceeding panels as differences in (C) observed linear growth rate and time to half maximum intensity. These values were derived from the regions shown in cyan shown in "B."  $N = 4-7$  and the individual traces used to derive the data in "C" are shown in *SI Appendix, Fig. S4*. \* $P < 0.05$ , \*\* $P < 0.01$ , \*\*\* $P < 0.001$ , and \*\*\*\* $P < 0.0001$  as calculated by the two-tailed  $t$  test with Welch's correction for unequal variance. (D) R256H ACTA1 has decreased nucleation and filament growth rate at  $2 \mu\text{M}$  G-actin. (Left graph) Number of filaments detected per unit time was used to calculate the nucleation rate using the Fiji plugin, FilamentDetector. Data obtained from 10 to 15 different focal fields from 2 to 3 replicates per condition.  $R^2$  for WT is 0.9853 and for R256H is 0.9924. (Middle images) R256H ACTA1 filaments are fewer in number and shorter in length. Image *Insets* are examples of fluorescent filaments at 1,000 s. Note that images were postprocessed for visualization purposes and used for manual filament measurements but not for automated tracking of number of filaments for calculating nucleation rate. (Right graph) Filament length measured by line segment analysis for 100 filaments per protein condition in ImageJ. Length converted to subunits based on approximately 370 actin subunits in  $1 \mu\text{m}$  (23).  $R^2$  for WT is 0.9970 and for R256H is 0.8741. For both graph slopes, \*\*\*\* $P < 0.0001$  by simple linear regression analysis in GraphPad Prism. Full focal field can be found in *SI Appendix, Fig. S5*. Scale bar represents  $5 \mu\text{m}$ . All error bars represent SEM.



critical concentration. Consistent with the decreased rate of filament growth that we observed by TIRF, we found that R256H ACTA1 had a higher critical concentration than WT ACTA1 (R256H 0.87  $\mu\text{M}$  [95% CI 0.67 to 1.0  $\mu\text{M}$ ] vs. WT 0.20  $\mu\text{M}$  [95% CI 0.15 to 0.26], *SI Appendix, Fig. S6*). Thus, our data show that R256H affects actin dynamics; however, our experiments cannot distinguish whether this is due to lower assembly rates or higher disassembly rates.

Our polymerization assays in Fig. 2 utilized either WT or R256H ACTA1; however, all of the DCM patients observed were heterozygous for the mutation and therefore express both WT and mutant ACTA1 (13). To test whether R256H ACTA1 has a dominant negative effect on polymerization (i.e., the mutant protein acts as a poison protein and prevents polymerization), we repeated our polymerization experiments with mixing of both proteins. If dominant negative effects of R256H ACTA1 were present, we would expect that adding 3  $\mu\text{M}$  R256H to 3  $\mu\text{M}$  WT protein would inhibit polymerization compared to 3  $\mu\text{M}$  WT alone. However, we saw that adding 3  $\mu\text{M}$  R256H to 3  $\mu\text{M}$  WT protein did not inhibit the polymerization kinetics compared to 3  $\mu\text{M}$  WT (*SI Appendix, Fig. S4E*). Moreover, we saw via TIRF microscopy that mixing WT and R256H ACTA1 resulted in intermediate nucleation and filament growth rates (*SI Appendix, Fig. S5 B and C*). This demonstrates that mutant protein is being integrated into filaments without preventing polymerization, and that the mutant protein is not acting through a dominant negative mechanism that poisons polymerization. Rather, the mutant has slow polymerization kinetics that are accelerated in the presence of WT ACTA1. Taken together, our results demonstrate that the R256H mutation affects both the stability and polymerization of actin.

**R256H ACTA1 Filaments Have Disrupted Actomyosin Interactions in the Presence of Thin Filament Regulatory Proteins.** Our polymerization experiments demonstrated that both WT and R256H actin can form filaments, and therefore, we set out to examine how the mutation affects the function of actin filaments interacting with binding partners. The force and power of muscle contraction is driven by the myosin molecular motor pulling on regulated thin filaments consisting of actin and the regulatory proteins troponin and tropomyosin (4). Given that *ACTA1*<sup>R256H/+</sup> patients have reduced cardiac contractility, we hypothesized that R256H ACTA1 filaments would alter myosin-based interactions with regulated thin filaments. To test our hypothesis, we used an in vitro motility assay in which fluorescently labeled actin/thin filaments are translocated over a bed of myosin in the presence of ATP and varying concentrations of calcium (27). For these experiments, we used porcine cardiac myosin (MYH7), which has biochemical and biophysical characteristics that are indistinguishable from human cardiac myosin (28–30). First, we examined whether the mutant protein affects the speed of actin translocation by myosin in the absence of regulatory proteins. We found that there was no difference in speed between WT and R256H ACTA1 filaments, demonstrating that cardiac myosin is capable of interacting with both WT or R256H ACTA1 filaments, and that the mutant protein does not affect the rate of myosin-based translocation (Fig. 3A, *Left* column pair).

Next, we examined whether the myosin-based translocation of actin is affected by the presence of the regulatory proteins troponin (Tn) and tropomyosin (Tm) (henceforth, collectively referred to as Tn/Tm). Tn and Tm bind to the actin filament, and they gate the calcium-dependent interactions between myosin and regulated thin filaments. We performed in vitro motility assays in the presence of human cardiac Tn/Tm for both WT and R256H ACTA1

filaments. Both WT and R256H ACTA1 filaments were nonmotile in the presence of Tn/Tm under low calcium conditions (pCa 9, Fig. 3A, *Middle* column pair) suggesting that Tn/Tm successfully inhibit actin–myosin interactions for both WT and mutant proteins at low calcium. Having confirmed Tn/Tm regulation of R256H ACTA1 at low calcium, we next wanted to test whether the inhibition of the Tn/Tm complex could be relieved under high calcium (pCa 4) conditions. Consistent with previous studies, WT ACTA1 thin filaments showed robust movement at pCa 4 (Fig. 3A, *Right* column pair, black outlined column representing WT ACTA1). Surprisingly, we found that R256H ACTA1 filaments remained nonmotile at pCa 4, and this speed was not different from pCa 9 (Fig. 3A, *Right* column pair, red outlined column representing R256H ACTA1). This is not due to an inability of myosin to interact with R256H actin, since these filaments move robustly in the absence of regulatory proteins (Fig. 3A). Taken together, our results reveal that R256H thin filaments show inhibited motile activity, only in the presence of regulatory proteins. This result was unexpected, since a similar effect has not previously been observed for cardiomyopathy-associated actin mutants.

All known patients with the R256H mutations are heterozygous for the mutation, and therefore express a mix of WT and mutant R256H. Moreover, ACTA1 protein is estimated to make up about 20% of the adult heart actin (ACTC1 is the major isoform in the heart) (31). As such, the mutant protein is likely expressed as a minority (~10%) of actin in the heart along with a mixture of other actin isoforms. Therefore, we assessed the dose dependence of the percent R256H ACTA1 on thin filament motility in the presence of Tn/Tm at pCa 4. To create filaments of various R256H ACTA1 concentrations, we mixed different concentrations of WT and R256H ACTA1 monomers which we subsequently polymerized (Fig. 3B). We found that 12.5% R256H ACTA1 was sufficient to reduce the speed of actin filaments in the presence of Tn/Tm at pCa 4.

While we see a clear reduction in the speed of thin filament translocation with increasing amounts of mutant protein at fully activating conditions (pCa 4), the heart generally works under subsaturating conditions (pCa 5–7). Therefore, we measured the full speed–calcium relationship for several mixtures containing mutant protein. The relationship between speed and pCa can be fitted with the Hill equation to derive maximum speed, minimum speed, calcium concentration at 50% maximum speed (pCa<sub>50</sub>), and cooperativity of activation. Because even 50% R256H ACTA1 results in nearly all filaments being nonmotile (Fig. 3B), we generated speed–pCa curves using 25% and 12.5% R256H ACTA1 so there were enough motile filaments for quantification (Fig. 3C and D). We found again that while the maximum speed under fully activating conditions decreased with increasing percentage of R256H ACTA1, the pCa<sub>50</sub> was unaffected by increasing amounts of mutant protein suggesting that the calcium sensitivity of activation is not decreased. In summary, we found that a small percentage of R256H ACTA1 is sufficient to inhibit biochemical contractility, but only in the presence of troponin and tropomyosin.

**R256H ACTA1 Filament Has Altered Positioning of the Tropomyosin-Interacting Residue K240.** Given the unexpected magnitude of inhibition of myosin-driven motility of R256H filaments only in the presence of Tn/Tm, we hypothesized that a structural change in the R256H filament alters interactions with regulatory proteins. High-resolution structures of the actin filament have revealed multiple charged residues in actin that specifically interact with tropomyosin (32–34). Given the changes

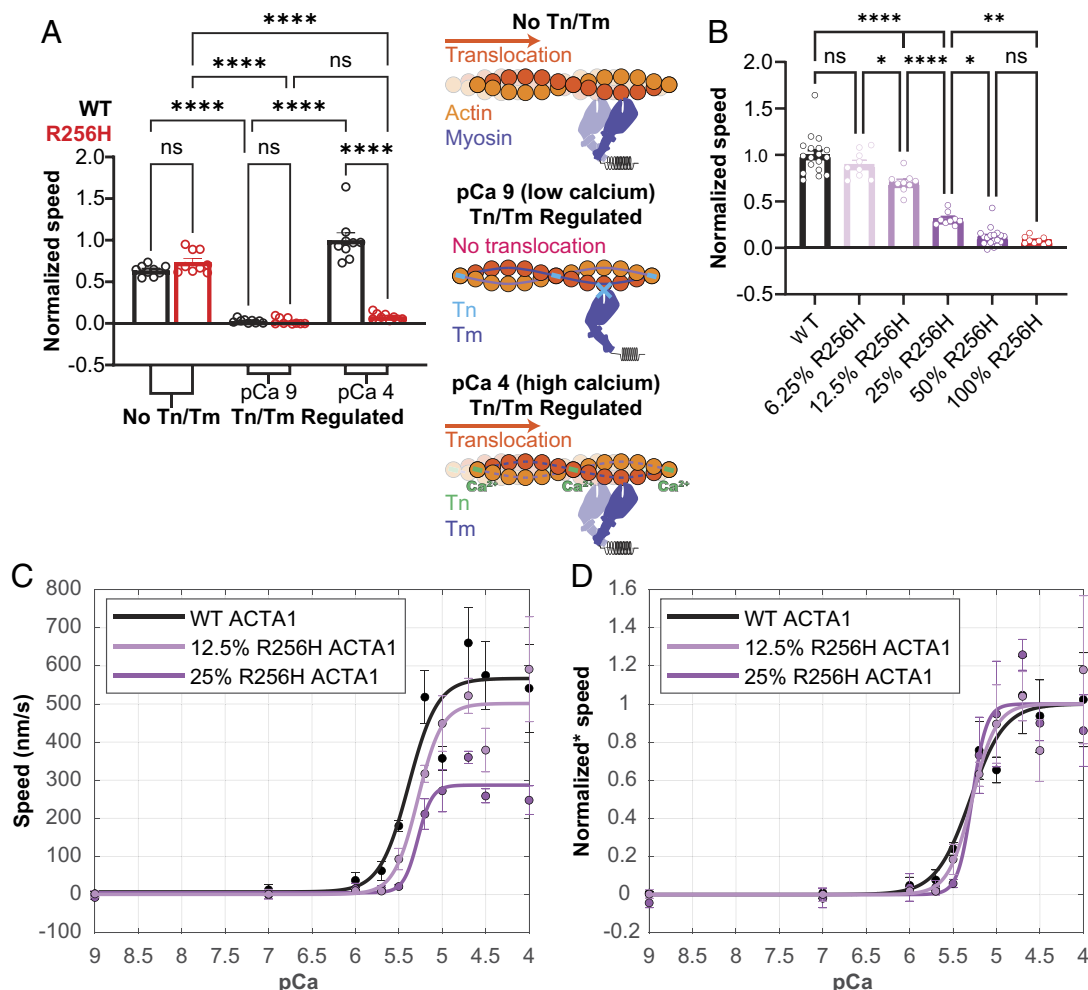


**Fig. 3.** ACTA1 R256H filaments have inhibited translocation by myosin only in the presence of Tn/Tm without affecting calcium sensitivity. (A) In vitro motility of either 100% WT or 100% R256H ACTA1 filaments with porcine cardiac myosin. Cartoons to the right of graphs are shown for conceptual visualization of the experiment. (Left column pair) In the absence of Tn/Tm, myosin freely translocates actin. There is no difference in speed between WT and R256H ACTA1 filaments. (Middle column pair) In the presence of Tn/Tm and under low calcium conditions, both WT and R256H ACTA1 filament speeds are arrested. This means that R256H ACTA1 filaments are capable of regulation by Tn/Tm. (Right column pair) In the presence of Tn/Tm and high calcium conditions, WT ACTA1 filament speeds are restored, but R256H ACTA1 filament speeds remain inhibited.  $N = 9$  for all conditions representing the average speed of all filaments in three focal fields quantified from three separate motility experiments. (B) Regulated in vitro motility experiments at pCa 4 (high calcium) of filaments containing various concentrations of ACTA1 R256H. As the concentration of ACTA1 R256H increases, the speed of filament translocation decreases. Note that 100% R256H data is reproduced from Fig. 3A. 100% WT from Fig. 3A is also reproduced but combined with additional replicates.  $N = 18$  for WT and 50% R256H while  $N = 9$  for all other conditions from 3 to 6 motility experiments.  $*P < 0.05$ ,  $**P < 0.01$ ,  $***P < 0.001$ , and  $****P < 0.0001$  as calculated by one-way ANOVA followed by multiple comparisons of every condition with either Šidák correction (A) or Tukey correction (B) as recommended by GraphPad Prism. Normalized speed means min/max normalization across all conditions. (C) pCa-speed response curves for 100% WT, 12.5% R256H ACTA1, and 25% R256H ACTA1 filaments. Data were fit with the Hill equation. Each point represents  $N = 6$  from two motility experiments. Absolute speeds are shown to demonstrate differences in maximum speed which are calculated as WT 567 nm/s (95% CI 437 to 698 nm/s), 12.5% R256H 501 nm/s (95% CI 408 to 595 nm/s), 25% R256H 287 nm/s (95% CI 408 to 595 nm/s). These differences are better demonstrated in the experiment in Fig. 3B. (D) Calcium sensitivity is unchanged for mutant-containing filaments. WT, 12.5% R256H, and 25% R256H  $pCa_{50}$  are 5.3 (95% CI 5.1 to 5.5), 5.3 (95% CI 5.1 to 5.5), and 5.3 (95% CI 5.1 to 5.5). Cooperativity has similarly overlapping 95% CI: WT cooperativity is 5.0 (95% CI 1.2 to 8.9), 12.5% R256H cooperativity is 7.2 (95% CI -0.2 to 14.6), and 25% R256H cooperativity is 12.1 (95% CI -7.1 to 31.5). Lines fit to the Hill equation have adjusted  $R^2$  of 0.89 for WT, 0.93 for 12.5% R256H, and 0.93 for 25% R256H. "Normalized\*" indicates min-max normalization within each condition as opposed to across all datasets as for other normalized data in figure.

in structure seen in the conformation of the actin monomer in the molecular dynamics simulations, we hypothesized that the mutation could affect residues in the actin filament involved in thin filament regulation.

To test this hypothesis, we used cryoelectron microscopy (cryo-EM) to determine the structures of both WT and R256H actin filaments bound to phalloidin. We used phalloidin to ensure stability of the mutant actin, since the mutant actin shows polymerization defects. It should be noted that phalloidin does not alter the natural conformations of the F-actin filament (35). Thus, we proceeded with resolving our WT and R256H filaments with phalloidin. We achieved 3.4 Å resolution for the WT and 3.3 Å resolution for the R256H mutant. At this resolution we could directly visualize the position of amino acid side chains. We found

that the WT and R256H ACTA1 electron density maps were nearly identical (Fig. 4A, "Combined"). Our refined WT and R256H ACTA1 structures aligned well with the published PDB 6T1Y structure (35) with global RMSDs of 0.532 and 0.553 Å, respectively. Despite the similarity between WT and R256H ACTA1 structures, there was a significant difference between the WT and mutant in the positioning of K240 (Fig. 4B). K240 (K238 by postcleavage numbering) is located near R256, and it plays a key role in interacting with tropomyosin in the myosin-bound state (SI Appendix, Fig. S7).

We aligned our structures to a published structure of actin bound with tropomyosin and myosin (PDB 8EFI) (36). There are no changes near the myosin binding interface, consistent with the unchanged myosin in vitro motility (SI Appendix, Fig. S7B);

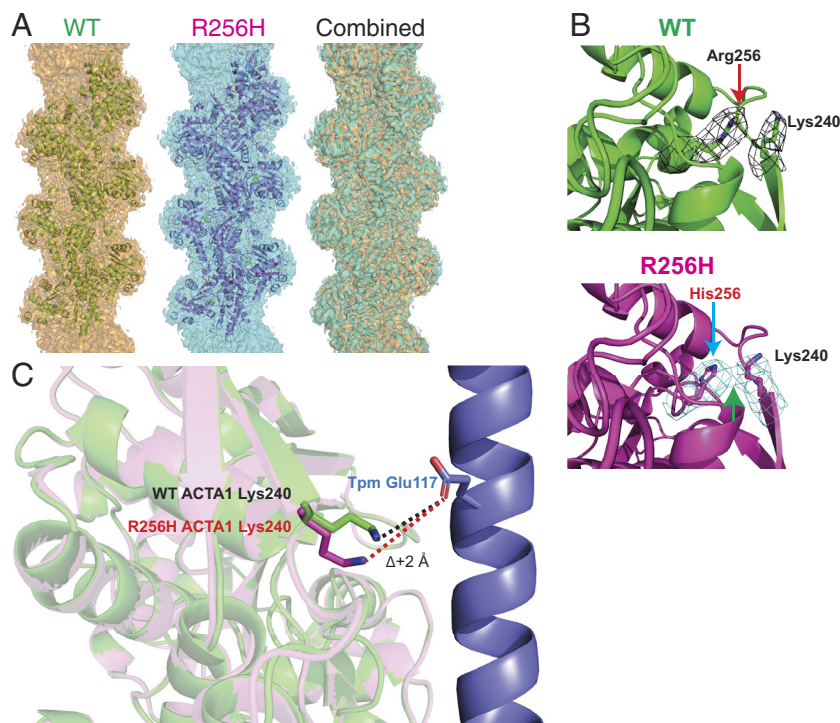


**Fig. 4.** R256H ACTA1 alters position of ACTA1 K240 which may disrupt interaction with Tpm E117. (A) WT and R256H ACTA1 have similar structures. Shown are cryo-EM densities at the 3σ contour level and superimposed atomic models rendered as cartoons for WT and R256H ACTA1. The cryo-EM densities of WT and R256H ACTA1 have substantial overlap as seen in the “Combined” figure. (B) Focused view of WT and R256H ACTA1 256 residue and K240 residue which are rendered as sticks while the remainder of the peptide backbone is rendered as a cartoon. The wire mesh represents the 5σ contour level of electron density surrounding each respective residue. Note how R256H ACTA1 K240 moves closer in proximity to His256 such that there is overlapping electron density between the two residues (green arrow) which is not present in WT ACTA1. (C) The change in Lys240 in R256H ACTA1 is predicted to cause an increase in distance between ACTA1 K240 and Tpm E117. Shown is the approximate position of tropomyosin E117 after aligning our atomic model to 8EF1 which contains a high-resolution structure of F-actin bound by myosin in rigor in the presence of Tpm. We show only the Tpm strand that interacts with ACTA1 K240 for clarity.

however, it is apparent that the change in position of K240 for the R256H filament results in K240 Nζ being about 2 Å further away from the ε-1 oxygen of E117 on tropomyosin which likely disrupts this interaction between actin and tropomyosin (Fig. 4C). The potential loss of the interaction between ACTA1 K240 and tropomyosin E117 in the activated, myosin-bound state of actin provides a potential link with the observed inhibition of myosin-induced R256H ACTA1 motility in the presence of Tn/Tm.

**ACTA1<sup>R256H/+</sup> Induced Cardiomyocytes Generate Less Force without Disrupting Calcium Transients and Demonstrate Sarcomere Disorganization.** While our biochemical and structural studies demonstrate that R256H ACTA1 affects contractility at the molecular scale, it is not clear whether these changes translate to altered contractility in cardiomyocytes. Therefore, we generated isogenic human-induced pluripotent stem cells (hPSCs) heterozygous for the ACTA1 R256H mutation using CRISPR/Cas9 (37). The parent wild type cells were shown by whole-exome sequencing to be free of any known genetic variants associated with familial cardiomyopathies (38). Two separate ACTA1<sup>R256H/+</sup> lines (referred to as “R256H clone 1” and “R256H clone 2” in supplementary figures) were created and independently compared to the parent wildtype isogenic line (referred to as “WT”). We differentiated our hPSCs to cardiomyocytes (hPSC-CMs) for at least 28 d prior to performing experiments using well-established protocols (39, 40). Data were acquired from at least two separate differentiations.

Altered contractility is a hallmark of DCM, and therefore we investigated whether the R256H mutation is sufficient to alter contraction. To measure cardiomyocyte contractility, we used traction force microscopy (TFM) by plating hPSC-CMs onto

10 kPa hydrogels containing embedded fluorescent beads. Cells were adhered to micropatterned extracellular matrix in a 7:1 aspect ratio as we have done previously (38). The 10 kPa hydrogel mimics physiological cardiac stiffness, and the 7:1 aspect ratio has been shown to improve sarcomere alignment, and both factors improve maturation (41). We found that ACTA1<sup>R256H/+</sup> hPSC-CMs produced less force than WT cells, demonstrating altered contractility in human cardiomyocytes due to an ACTA1 mutation (Fig. 5A and B).

While reduced contractility in the mutant cells is consistent with the observed molecular defects, there are multiple other downstream mechanisms that could also contribute to the reduced contractility seen in the mutant cells, including alterations in the calcium transient, sarcomeric organization, cell size, and/or changes in the structure/function of the thin filaments. Therefore, we tested these possibilities. First, we manually traced cell edges, and we did not detect a change in size between ACTA1<sup>R256H/+</sup> and WT cells (Fig. 5C). Next, we measured the calcium transients in mutant cells, since reduced calcium transients could contribute to reduced contractility. We found that overall calcium transient duration was increased (Fig. 5D and E), which would be expected to increase, not decrease contractility. However, the net calcium flux, calculated as the integral of the calcium transient from ΔF/F<sub>0</sub>, was not significantly different between the WT and the mutant, indicating the overall amount of calcium moving into the cytoplasm is similar between both WT and R256H (Fig. 5F). These data suggest that alterations in calcium handling do not explain the ACTA1 R256H cardiomyocyte hypocontractility phenotype. Finally, we used immunofluorescence to measure the alignment of sarcomeres in the cells, since alignment of the sarcomere



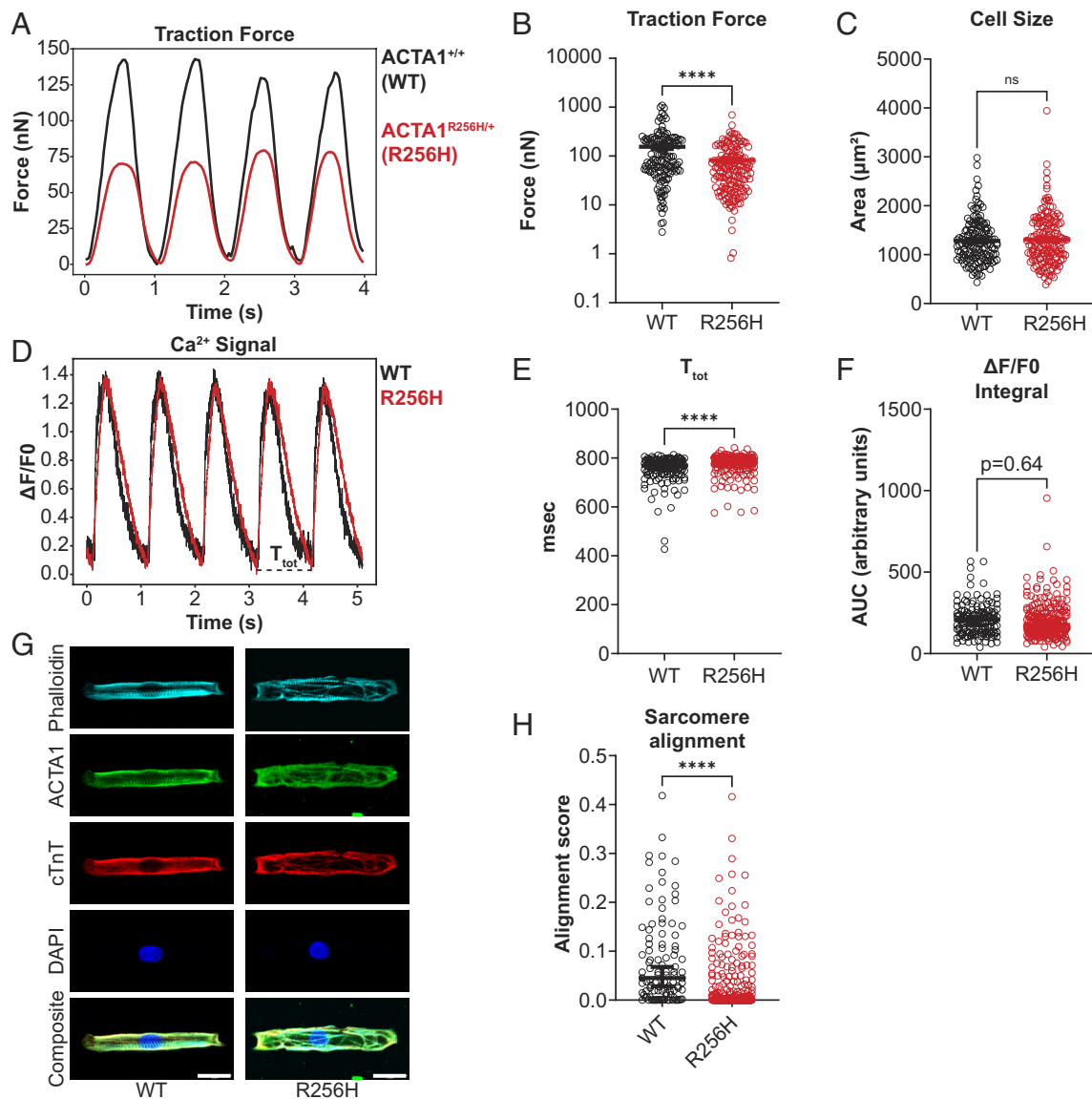


**Fig. 5.** ACTA1<sup>R256H/+</sup> hPSC-CMs exhibit reduced force without a change in calcium flux but have disordered sarcomeres. (A) Representative force trace of a single paced WT and ACTA1<sup>R256H/+</sup> hPSC-CM (referred to as “R256H”) demonstrating reduced force produced by mutant cells as determined by traction force microscopy. (B) Summary of quantified force (WT mean force 155.2 nN vs. R256H mean force 82.3 nN) and (C) area (WT mean 1,280 μm<sup>2</sup> vs. R256H mean area 1,310 μm<sup>2</sup>) for individual hPSC-CMs. \*\*\*\**P* < 0.0001 as calculated by the two-tailed nonparametric Mann-Whitney *t* test. WT *N* = 139 and R256H *N* = 149 from at least three separate differentiations. (D) Representative Ca<sup>2+</sup> traces using FLUOFORTE from cells paced at 1 Hz. Dashed lines denote the time values quantified for (E) the total time of calcium transient (T<sub>tot</sub>) with WT mean of 750 ms and R256H mean of 777 ms. (F) Calcium flux (integral of ΔF/F<sub>0</sub> signal) is not different. WT *N* = 120 and R256H *N* = 226 from at least two separate differentiations. \*\*\*\**P* < 0.0001 as calculated by nonparametric Mann-Whitney and parametric *t* tests for “E” and “F” respectively. (G) *P*-value calculated by the parametric *t* test. Note that points for “E” and “G” are spread horizontally to try to minimize overlap. (H) Examples of patterned hiPSC-CMs stained for different structures. ACTA1-specific antibody is validated in *SI Appendix, Fig. S2C*. Phalloidin binds all polymerized actin (F-actin). (Scale bar, 25 μm.) (H) Sarcomere alignment scores processed from phalloidin images using SotaTool. WT mean alignment score of 0.080 and R256H mean alignment score 0.032. A higher score corresponds to more alignment of Z-discs within the cell. WT *N* = 99 and R256H *N* = 258 from at least two separate differentiations. \*\*\*\**P* < 0.0001 calculated by the nonparametric Mann-Whitney *t* test. All error bars represent SEM though some are not visible due to the high density of points. Mutant cell data obtained from two separate clones, and the separated data can be found in *SI Appendix, Fig. S8*.

is important for optimized force production (Fig. 5G). First, we identified successfully differentiated cells based on staining with cardiac troponin T (cTnT), a specific marker of cardiomyocytes (6). We also verified the presence and localization of ACTA1 to the sarcomere using an ACTA1 specific antibody (validated in *SI Appendix, Fig. S2C*) and dual-staining with phalloidin which is specific for F-actin. We clearly observe the integration of ACTA1 in the sarcomere. Moreover, we observed that ACTA1<sup>R256H/+</sup> hPSC-CMs appear to have sarcomeric arrays that were less aligned with the longitudinal cell axis compared to WT. We quantified the alignment using the SarcOmere Texture Analysis algorithm (SotaTool) which mathematically scores sarcomere alignment on a scale between 0 and 1, with higher alignment corresponding to

a higher score (42). Consistent with our observations, WT cells had a significantly higher alignment score than ACTA1<sup>R256H/+</sup> hPSC-CMs (Fig. 5H). Taken together, our results show that the mutant has reduced force production at the cellular level, consistent with our molecular phenotype. We did not detect changes in the calcium transient or cell size that could potentially contribute to this phenotype, but we did see changes in sarcomeric organization which could also contribute to decreased force.

## Discussion

Due to ACTA1's high levels of expression in skeletal muscle, its mutations have been largely studied in the context of skeletal



myopathies, and hundreds of dominant actin missense variants and a smaller fraction of recessive variants have been associated with skeletal muscle diseases. Recently, ACTA1 variants were identified in patients with DCM; however, ACTA1 only makes up ~20% of the actin in the heart (31), and it has been unclear whether or how these mutations impact cardiac contractility. Here, we performed a multiscale study of a cardiomyopathy-associated ACTA1 variant, R256H, which revealed fundamental connections between structure, molecular dysfunction, and altered cardiomyocyte contractility. We used molecular dynamics simulations to show that R256H mutant actin monomers have decreased nucleotide binding stability which we corroborate biochemically. To explore the functional implications of reduced nucleotide binding, we successfully purified recombinant WT and mutant ACTA1. We find that R256H ACTA1 has lower thermal stability and slower polymerization kinetics. Moreover, R256H potentially disrupted actin–myosin translocation speeds only in the presence of actin regulatory proteins. We could observe the inhibitory effects of the mutant protein at likely physiological levels of mutant protein. We used cryo-EM to determine a high-resolution structure of R256H ACTA1, and we found an altered residue that likely disrupts an interaction with tropomyosin that is important for thin filament activation. Finally, we introduced the ACTA1 R256H mutation in hPSC-CMs and show that this disrupts force production and sarcomeric architecture. Taken together, our work demonstrates how an ACTA1 mutation can reduce cardiomyocyte contractility across multiple scales of organization, even at low levels of expression.

#### Elucidating the Primary Driver of R256H ACTA1 Hypocontractility.

To date, several variants in ACTA1 associated with skeletal myopathies have been characterized, and these mutations have shown a wide spectrum of defects in protein stability, polymerization, and actomyosin interactions (43–45). While the exact levels of ACTA1 mutant protein have not been measured in patient hearts, it is informative to do back-of-the-envelope calculations. ACTA1 makes up ~20% of the actin in the heart, and the patients were heterozygous for the R256H mutation. Since R256H ACTA1 appears to cause DCM in an autosomal dominant manner (13), this suggests that ~10% mutant protein in the heart is sufficient to cause disease. As such, mutations in ACTA1 associated with cardiomyopathies likely have large impacts on protein function, and we would expect to see impacts on function even at low expression levels. Consistent with our estimations, we found that R256H ACTA1 causes several dose-dependent changes in actin function at the molecular scale including changes in thin filament regulation and polymerization. It is also worth noting that ACTA1 expression increases in DCM, which likely increases R256H ACTA1 expression above 10% of total actin and could establish a feed forward loop of worsening cardiomyopathy (31).

Our data clearly show that molecular contractility is inhibited for R256H in the presence of the actin regulatory proteins troponin and tropomyosin, even at very low concentrations (~10%) of mutant protein (Fig. 3). This suggests that even small amounts of R256H expressed in the heart could affect contractility. To our knowledge, no other cardiomyopathy-associated actin mutation shows complete arrest of thin filament movement only in the presence of the Tn/Tm regulatory complex. Interestingly, other noncardiomyopathy associated mutations in the same region of actin show a similar decrease in actin translocation speeds by myosin in the presence of tropomyosin. The D294V ACTA1 mutation, associated with severe congenital skeletal muscle fiber type disproportion, had a similarly dramatic effect of completely abrogating actin filament translocation with the *in vitro* motility assay

regulated by tropomyosin (45). Additionally, the R258H ACTA2 (smooth muscle actin) mutation associated with thoracic aortic aneurysms also shows decreased actomyosin translocation speeds in the presence of tropomyosin (23). Taken together, we believe that the reduced speed of thin filaments by myosin in the presence of regulatory Tn/Tm is a primary driver of hypocontractility.

Interestingly, we only observe inhibition of motility in the presence of the regulatory proteins, suggesting that the mutation does not directly affect the kinetics of actin's interaction with myosin. The regulation of actin and myosin binding by Tn/Tm has a well-established structural basis (33). Thus, we hypothesized that the R256H mutant would have an associated structural change in the actin filament that could affect regulation. Using cryo-EM, we solved a high-resolution structure and built an atomic model of ACTA1 R256H (Fig. 4). The R256H mutation causes K240 to move closer to H256, evidenced by an increase in electron density between these residues. We believe that the loss of the positively charged arginine when substituting with histidine allows K240 to move closer to residue 256. Importantly, it has previously been shown that K240 forms a specific interaction with the E117 residue on tropomyosin in the myosin-bound state (Fig. 4C) (36). Thus, we speculate that the loss of this interaction decreases the favorability of the tropomyosin open state, potentially contributing to our observed decreases in contractility. Consistent with this notion, the E117K mutation in tropomyosin causes congenital skeletal myopathy, and biochemical studies show that this mutation causes reduced thin filament activation associated with hypocontractility (46, 47). Notably, the prior structure of tropomyosin in the myosin-bound state did not resolve the structure of tropomyosin beyond residue 210. Another study which obtained a high-resolution structure of F-actin with tropomyosin and the troponin complex under low calcium conditions shows additional interactions between actin K240 and tropomyosin residues E240 and D275 (48). Whether these interactions are also disrupted with R256H ACTA1 remains to be seen. Ultimately, a structure of R256H ACTA1 complexed with tropomyosin is needed to better understand which interactions between R256H ACTA1 and tropomyosin are affected.

In addition to altering thin filament regulation, our data clearly demonstrate that R256H alters nucleotide binding, stability of actin monomers, and decreases polymerization rates. Our molecular dynamics simulations predict that R256H could affect nucleotide binding (Fig. 1B) which is corroborated biochemically (Fig. 1D). Importantly, nucleotide binding has been shown to be critical for the stability of actin monomers and polymerization kinetics (24). Accordingly, R256H shows decreased thermal stability and defective polymerization (Fig. 2). Unstable protein can either lead to decreased protein levels, indicating haploinsufficiency, or misfolding and aggregation which may contribute to pathogenicity (49). Haploinsufficiency of ACTA1 has not been shown to cause disease based on the lack of cardiac phenotype of *Acta1*<sup>+/-</sup> mice (50). However, it should be noted that these mice do not have reduced *Acta1* transcripts, so it is possible that reducing *Acta1* at the mRNA and protein levels may still produce a haploinsufficiency phenotype that has yet to be uncovered. While unstable protein can lead to protein aggregation, potentially contributing to pathogenicity, we did not observe protein aggregates in our *ACTA1*<sup>R256H/+</sup> hPSC-CMs making this possibility less likely. Thus, it is difficult to directly connect decreased R256H stability to hypocontractility. Moreover, loss of nucleotide has been shown to dramatically decrease actin polymerization kinetics (24). Consistent with this notion, we find that R256H polymerization kinetics are severely reduced, especially the nucleation rate (Fig. 2). However, R256H does not inhibit the polymerization kinetics of

WT ACTA1 when mixed together (*SI Appendix, Fig. S4*). Having ~10% polymerization-defective actin seems unlikely to affect the overall thin filament length in cardiomyocytes, though further work will be needed to test this hypothesis.

**hPSC-CMs with R256H ACTA1 Are Hypocontractile with Disrupted Sarcomeric Organization.** The hallmark of DCM is reduced ejection fraction, which is a hypocontractile state. We and others have shown that hPSC-CMs harboring DCM-causing mutations in sarcomeric proteins exhibit reduced force or stress production (38, 51–57). Consistent with this notion, *ACTA1*<sup>R256H/+</sup> hPSC-CMs show reduced force production without significant changes in calcium handling (Fig. 5 *A–F*). This provides direct evidence that ACTA1 mutations, which are usually associated with skeletal myopathies, can affect human cardiomyocyte contractility.

We and others previously found that DCM-associated mutations in hPSC-CMs cause increased cell size, but this was not the case for *ACTA1*<sup>R256H/+</sup> hPSC-CMs (38, 57). However, consistent with our studies with cardiac troponin T, we did find cells had sarcomere misalignment (Fig. 5 *G* and *H*). Defects in ACTA1 polymerization have been linked to skeletal myopathies and are thought to be partly driven by changes in thin filament length (58). Changes in thin filament length in cardiac tissues have also been linked to cardiomyopathy, which was seen with deletion of the cardiac-enriched actin nucleation factor, Leiomodin 2 (*Lmod2*) (59, 60). It is possible that the polymerization defects seen with R256H could contribute to the sarcomeric disarray seen here.

#### **ACTA1 Mutations in Cardiomyopathy and Skeletal Myopathy.**

Our data collectively show biochemical and cellular evidence of cardiomyocyte hypocontractility in the presence of R256H ACTA1. Another important question is whether R256H ACTA1 impacts skeletal muscle function. Of the 3 patients with the R256H variant, none had gross clinical features of skeletal myopathy (13). This was a surprising finding given the much higher expression of ACTA1 in skeletal muscle compared to the heart (6). The lack of a skeletal muscle phenotype is even more unexpected taken together with our in vitro motility data that show 12.5% R256H ACTA1 is sufficient to disrupt actin–myosin translocation speeds in the presence of Tn/Tm (Fig. 3*B*). In *ACTA1*<sup>R256H/+</sup> skeletal muscle, mutant actin could be as high as 50% which in our in vitro motility assay results in arrested filament movement.

We speculate about two possibilities how a skeletal muscle phenotype may be absent. First, our data show that R256H ACTA1 has profoundly reduced polymerization kinetics, especially its nucleation rate. It is possible that less R256H ACTA1 is incorporated into skeletal muscle than cardiac thin filaments due to different factors governing polymerization in skeletal and heart muscles. There are some thin filament proteins that are uniquely expressed in either skeletal or cardiac muscle. Leiomodins (*LMODs*) are important nucleation factors in striated muscle and exist in 3 isoforms: *LMOD1–3* (61). *LMOD2* is predominantly expressed in the heart and may allow for more incorporation of R256H ACTA1 into cardiac thin filaments compared to skeletal muscle thin filaments. Notably, a published crystal structure of *LMOD2* with actin shows interactions of leiomodin with actin subdomain 2 (62), and our molecular dynamics simulations of the R256H G-actin show changes in this region (*SI Appendix, Fig. S1*). Similarly, nebulin plays a critical role in regulating skeletal muscle thin filaments, and several ACTA1 residues in subdomain 4, where R256H is located, are predicted to form contacts with nebulin based on the recently resolved cryoelectron tomography structure of myofibrils with nebulin (63). Finally, cardiac

and skeletal muscles express different tropomyosin isoforms in different abundance (64). Different tropomyosin isoforms affect actin polymerization differently providing a possible explanation to differential incorporation of WT and R256H ACTA1 in cardiac and skeletal muscles (65). Second, our data show decreased thermal stability for R256H ACTA1. Alternatively, it is possible R256H ACTA1 has greater stability in cardiac muscle leading to more mutant protein in cardiac filaments. Regardless, future studies to probe more deeply into the differences in the cardiac and skeletal muscle phenotypes of R256H ACTA1, skeletal muscle models of R256H ACTA1 are needed.

There are several other variants in ACTA1 that have been linked with both DCM (9–12) and skeletal myopathy. However, there was a recent report of an ACTA1 G253S variant that may, like R256H, cause DCM without a clinically apparent skeletal myopathy (14). We believe it will be important to apply the multiscale framework demonstrated here to further explore these ACTA1 mutations to see whether these mutations have similarly potent effects on actin function like R256H.

## **Conclusions**

We define the likely mechanistic basis for the low-expression ACTA1 isoform causing cardiomyocyte hypocontractility. We demonstrate that the R256H ACTA1 mutation induces hypocontractility by potentially disrupting actomyosin translocation in the presence of the thin filament regulatory proteins troponin and tropomyosin. Importantly, we show that ~10% R256H ACTA1 protein is sufficient to cause molecular hypocontractility. We link our molecular hypocontractility to a structural change in R256H ACTA1 filaments that could alter the interaction between ACTA1 K240 and tropomyosin E117. We find additional defects in R256H ACTA1 nucleotide binding, monomer stability, and polymerization kinetics which may further contribute to pathology. We also show that an ACTA1 mutation can cause cardiomyocyte hypocontractility. Taken together, our work demonstrates that ACTA1 mutations have a role in cardiomyopathy and lays the foundation for future studies into ACTA1 mutations associated with cardiomyopathy.

## **Materials and Methods**

Detailed methods can be found in *SI Appendix*.

**Molecular Dynamics.** Simulations were performed similar to previous ACTC1 simulations (16). Each simulation was done five times for 1  $\mu$ s with G-ACTA1 (PDB 1J6Z) (17) using NAMD 3.0 alpha and the CHARMM36 forcefield (66, 67). Data were analyzed using the MDAnalysis Python package (68, 69).

**Recombinant ACTA1 Purification.** We adapted a SF9/baculovirus system that has been successfully used to produce other muscle actins including mutant actins (18–21). We used the Bac-to-Bac system (Thermo Fisher Scientific) to express recombinant proteins either cloned from mammalian cDNA or created with synthetic nucleotides. After expression, cells were lysed, clarified, and then applied to a HisPur column (Thermo Fisher Scientific) with washing. The His tag was removed, and recombinant actin protein was eluted off the column by cleavage with chymotrypsin followed by additional purification by polymerization/depolymerization.

**Actin ATP Exchange Experiment.** We measured the exchange of ATP into ADP-bound ACTA1 in which ADP-actin undergoes exchange with fluorescent eATP (70). We calculated exchange kinetics by measuring fluorescence.

**Thermal Shift Assay.** All thermal shift experiments were performed using the Protein Thermal Shift Dye Kit (Thermo Fisher Scientific) and following the standard commercial protocol with an Applied Biosystems QuantStudio 3 Real-Time PCR system.

**Pyrene-Actin Polymerization Fluorescence Assay.** Rabbit ACTA1 was pyrene labeled, and polymerization experiments were performed as previously described (71, 72). Briefly, recombinant ACTA1 was mixed with pyrene-labeled ACTA1 under high salt conditions and polymerization kinetics were calculated from fluorescent signal. Critical concentration experiments using pyrene-actin were performed by measuring steady-state pyrene-actin fluorescence signal after 24 h as described previously (73).

**TIRF Analysis of Fluorescent-Labeled ACTA1.** A subset of rabbit ACTA1 was Alexa Fluor 647 labeled and another subset of rabbit ACTA1 was biotinylated as previously described (72). Kinetic experiments were performed by mixing recombinant ACTA1 with fluorescently labeled ACTA1 in the presence of biotinylated-ACTA1 (to allow polymerizing filaments to adhere to the coverslip) and measuring the changing length of fluorescent filaments.

**In Vitro Motility Assay.** Porcine cardiac myosin and actin purification, and preparation of recombinant human cardiac tropomyosin and troponin were performed as we have described previously (38). The gliding speed of phalloidin-stabilized fluorescent ACTA1 filaments over a bed of myosin was measured with or without tropomyosin and troponin and under various calcium conditions.

**Cryo-EM.** We utilized methods similar to prior (74–76). Recombinant protein was polymerized and stabilized with phalloidin followed by plunge freezing, electron microscopy, model assembly using an initial F-actin structure (PDB 6T1Y) (35), and then model refinement. Structure analysis was performed using PyMOL.

**hPSC Line Derivation, Maintenance, and hPSC-CM Differentiation.** ACTA1<sup>R256H/+</sup> hPSCs were derived by the Genome Engineering and iPSC Center (GEIC) at Washington University in St. Louis, cultured, and differentiated using modifiers of WNT signaling with metabolic selection as detailed before (38).

**Traction Force Microscopy.** Traction force microscopy was performed on patterned 10 kPa hydrogels as previously described (38, 57, 77). Analysis was done using Contrax software (41, 78)

**Measurement and Analysis of Calcium Transients in Live Cells.** We performed calcium transient imaging as previously except with a different calcium indicator dye, FLUOFORTE. Data were analyzed with CalTrak (77, 79).

**Immunofluorescence Staining and Measurement of Sarcomere Alignment.** Immunostaining was performed similar to prior (38), and SotaTool was used to calculate sarcomere alignment (42).

**Data, Materials, and Software Availability.** All data supporting the findings of this study are deposited in the Johns Hopkins Research Data Repository and can be accessed at <https://doi.org/10.7281/T1/MX05CQ> (80). Structures for phalloidin-stabilized wildtype ACTA1 and R256H ACTA1 F-actin have been deposited in the Protein Data Bank (PDB) and EM Data Bank (EMD). The accession codes for wildtype ACTA1 are PDB 9DUU (81) and EMD-47179 (82). The accession codes for R256H ACTA1 are PDB 9DUV (83) and EMD-47180 (84).

**ACKNOWLEDGMENTS.** We thank Patricia Fagnant and Kathleen Trybus at the University of Vermont for discussions regarding recombinant actin purification. We thank Teresa Naismith and DeHaven McCray at Washington University in St. Louis for their respective help with actin purification and TIRF microscopy fluorescent actin polymerization experiments. We thank Katherine Basore and Brock Summers at the Washington University Center for Cellular Imaging (WUCCI) for preparing the cryo-EM samples and collecting the data which was funded through the Department of Biochemistry and Molecular Biophysics Seed Grant (to A.G., R.Z., and M.J.G.). We would also like to thank Vitold Galkin at Eastern Virginia Medical School for discussion regarding the F-actin structure. We would like to acknowledge the GEIC at Washington University in St. Louis for creation of our hPSC line which was partly funded by the Washington University School of Medicine in St. Louis Institute of Clinical and Translational Science Just-In-Time Core Usage Funding Program (JIT744 to A.G. and M.J.G.). Finally, we thank Anjali Owens at the University of Pennsylvania for clinical discussions regarding the ACTA1 R256H mutation. This work was supported by the NIH (T32 HL007081, T32 HL007227, and K08 HL173569 to A.G.; R01 GM138448 to S.J.; R01 GM138854 to R.Z.; R01 HL141086 to M.J.G.; R01 HL138466, R01HL139714, R01 HL151078, and R35 HL161185 to K.J.L.); the Leducq Foundation Network (20CVD02 to K.J.L.); the Burroughs Wellcome Fund (1014782 to K.J.L.); the Children's Discovery Institute of Washington University and St. Louis Children's Hospital (CH-II-2015-462, CH-II-2017-628 to K.J.L.; PM-LI-2019-829 to K.J.L. and M.J.G.); the WUCCI (CDI-CORE-2015-505 to M.J.G.); the Foundation of Barnes-Jewish Hospital (8038-88 to K.J.L.). K.J.L. reports consulting agreements from Implicit Biosciences, Cytokinetics, Medtronic, Kiniksa Pharmaceuticals, and SUN Pharmaceuticals.

1. E. M. Hsich *et al.*, Heart transplantation: An in-depth survival analysis. *JACC Heart Fail* **8**, 557–568 (2020).
2. E. M. McNally, L. Mestroni, Dilated cardiomyopathy: Genetic determinants and mechanisms. *Circ. Res.* **121**, 731–748 (2017).
3. L. Escobar-Lopez *et al.*, Association of genetic variants with outcomes in patients with nonischemic dilated cardiomyopathy. *J. Am. Coll. Cardiol.* **78**, 1682–1699 (2021).
4. A. Garg, K. J. Lavine, M. J. Greenberg, Assessing cardiac contractility from single molecules to whole hearts. *JACC: Basic Transl. Sci.* **9**, 414–439 (2023).
5. M. A. Burke, S. A. Cook, J. G. Seidman, C. E. Seidman, Clinical and mechanistic insights into the genetics of cardiomyopathy. *J. Am. Coll. Cardiol.* **68**, 2871–2886 (2016).
6. M. Uhlen *et al.*, Proteomics. Tissue-based map of the human proteome. *Science* **347**, 1260419 (2015).
7. E. A. Despond, J. F. Dawson, Classifying cardiac actin mutations associated with hypertrophic cardiomyopathy. *Front. Physiol.* **9**, 405 (2018).
8. B. Ilkovski, S. Clement, C. Sewry, K. N. North, S. T. Cooper, Defining alpha-skeletal and alpha-cardiac actin expression in human heart and skeletal muscle explains the absence of cardiac involvement in ACTA1 nemaline myopathy. *Neuromuscul. Disord.* **15**, 829–835 (2005).
9. R. Gatayama *et al.*, Nemaline myopathy with dilated cardiomyopathy in childhood. *Pediatrics* **131**, e1986–e1990 (2013).
10. K. Tadokoro *et al.*, Congenital myopathy with fiber-type disproportion accompanied by dilated cardiomyopathy in a patient with a novel p. G48A ACTA1 mutation. *J. Neurol. Sci.* **393**, 142–144 (2018).
11. A. Matsumoto *et al.*, A case of congenital fiber-type disproportion syndrome presenting dilated cardiomyopathy with ACTA1 mutation. *Mol. Genet. Genomic. Med.* **10**, e2008 (2022).
12. X. Lornage *et al.*, Asymmetric muscle weakness due to ACTA1 mosaic mutations. *Neurology* **95**, e3406–e3411 (2020).
13. N. Reza *et al.*, ACTA1 novel likely pathogenic variant in a family with dilated cardiomyopathy. *Circ. Genom. Precis. Med.* **11**, e002243 (2018).
14. A. Diaz Exposito, A. Robles Mezcuca, A. I. Perez Cabeza, J. M. Garcia Pinilla, A new mutation in the ACTA1 gene possibly associated with dilated cardiomyopathy without concomitant myopathy. *Rev. Esp. Cardiol. (Engl. Ed.)* **75**, 850–852 (2022).
15. R. Dominguez, K. C. Holmes, Actin structure and function. *Annu. Rev. Biophys.* **40**, 169–186 (2011).
16. M. C. Viswanathan *et al.*, A role for actin flexibility in thin filament-mediated contractile regulation and myopathy. *Nat. Commun.* **11**, 2417 (2020).
17. L. R. Otterbein, P. Graceffa, R. Dominguez, The crystal structure of uncomplexed actin in the ADP state. *Science* **293**, 708–711 (2001).
18. P. Anthony Akkari *et al.*, Production of human skeletal alpha-actin proteins by the baculovirus expression system. *Biochem. Biophys. Res. Commun.* **307**, 74–79 (2003).
19. P. B. Joel, P. M. Fagnant, K. M. Trybus, Expression of a nonpolymerizable actin mutant in Sf9 cells. *Biochemistry* **43**, 11554–11559 (2004).
20. A. H. Iwane, M. Morimatsu, T. Yanagida, Recombinant alpha-actin for specific fluorescent labeling. *Proc. Jpn. Acad. Ser. B Phys. Biol. Sci.* **85**, 491–499 (2009).
21. M. M. Mundia, R. W. Demers, M. L. Chow, A. A. Perieteanu, J. F. Dawson, Subdomain location of mutations in cardiac actin correlate with type of functional change. *PLoS One* **7**, e36821 (2012).
22. D. J. Kast, S. Jansen, Purification of modified mammalian actin isoforms for in vitro reconstitution assays. *Eur. J. Cell Biol.* **102**, 151363 (2023).
23. H. Lu, P. M. Fagnant, C. S. Bookwalter, P. Joel, K. M. Trybus, Vascular disease-causing mutation R258C in ACTA2 disrupts actin dynamics and interaction with myosin. *Proc. Natl. Acad. Sci. U.S.A.* **112**, E4168–E4177 (2015).
24. E. M. De La Cruz, T. D. Pollard, Nucleotide-free actin: Stabilization by sucrose and nucleotide binding kinetics. *Biochemistry* **34**, 5452–5461 (1995).
25. S. Z. Chou, T. D. Pollard, Cryo-electron microscopy structures of pyrene-labeled ADP-P(i)- and ADP-actin filaments. *Nat. Commun.* **11**, 5897 (2020).
26. L. K. Doolittle, M. K. Rosen, S. B. Padrick, Measurement and analysis of in vitro actin polymerization. *Methods Mol. Biol.* **1046**, 273–293 (2013).
27. S. J. Kron, J. A. Spudich, Fluorescent actin filaments move on myosin fixed to a glass surface. *Proc. Natl. Acad. Sci. U.S.A.* **83**, 6272–6276 (1986).
28. M. J. Greenberg, H. Shuman, E. M. Ostap, Inherent force-dependent properties of  $\beta$ -cardiac myosin contribute to the force-velocity relationship of cardiac muscle. *Biophys. J.* **107**, L41–L44 (2014).
29. J. Sung *et al.*, Harmonic force spectroscopy measures load-dependent kinetics of individual human beta-cardiac myosin molecules. *Nat. Commun.* **6**, 7931 (2015).
30. J. C. Deacon, M. J. Bloemink, H. Rezavandi, M. A. Geeves, L. A. Linwand, Identification of functional differences between recombinant human alpha and beta cardiac myosin motors. *Cell Mol. Life Sci.* **69**, 2261–2277 (2012).
31. Y. C. Chen *et al.*, Effective top-down LC/MS+ method for assessing actin isoforms as a potential cardiac disease marker. *Anal. Chem.* **87**, 8399–8406 (2015).
32. J. von der Ecken *et al.*, Structure of the F-actin-tropomyosin complex. *Nature* **519**, 114–117 (2015).
33. Y. Yamada, K. Namba, T. Fujii, Cardiac muscle thin filament structures reveal calcium regulatory mechanism. *Nat. Commun.* **11**, 153 (2020).
34. C. Risi *et al.*, High-resolution cryo-EM structure of the cardiac actomyosin complex. *Structure* **29**, 50–60.e4 (2021).
35. S. Pospisil, F. Merino, S. Raunser, Structural effects and functional implications of phalloidin and jasplakinolide binding to actin filaments. *Structure* **28**, 437–449.e5 (2020).



36. M. H. Doran *et al.*, Myosin loop-4 is critical for optimal tropomyosin repositioning on actin during muscle activation and relaxation. *J. Gen. Physiol.* **155**, e202213274 (2023).
37. M. Jinek *et al.*, A programmable dual-RNA-guided DNA endonuclease in adaptive bacterial immunity. *Science* **337**, 816–821 (2012).
38. S. R. Clippinger *et al.*, Disrupted mechanobiology links the molecular and cellular phenotypes in familial dilated cardiomyopathy. *Proc. Natl. Acad. Sci. U.S.A.* **116**, 17831–17840 (2019).
39. X. Lian *et al.*, Robust cardiomyocyte differentiation from human pluripotent stem cells via temporal modulation of canonical Wnt signaling. *Proc. Natl. Acad. Sci. U.S.A.* **109**, E1848–E1857 (2012).
40. X. Lian *et al.*, Directed cardiomyocyte differentiation from human pluripotent stem cells by modulating Wnt/beta-catenin signaling under fully defined conditions. *Nat. Protoc.* **8**, 162–175 (2013).
41. A. J. Ribeiro *et al.*, Contractility of single cardiomyocytes differentiated from pluripotent stem cells depends on physiological shape and substrate stiffness. *Proc. Natl. Acad. Sci. U.S.A.* **112**, 12705–12710 (2015).
42. J. M. Stein *et al.*, Software tool for automatic quantification of sarcomere length and organization in fixed and live 2D and 3D muscle cell cultures in vitro. *Curr. Protoc.* **2**, e462 (2022).
43. N. G. Laing *et al.*, Mutations and polymorphisms of the skeletal muscle alpha-actin gene (ACTA1). *Hum. Mutat.* **30**, 1267–1277 (2009).
44. J. J. Feng, S. Marston, Genotype-phenotype correlations in ACTA1 mutations that cause congenital myopathies. *Neuromuscul. Disord.* **19**, 6–16 (2009).
45. N. F. Clarke *et al.*, The pathogenesis of ACTA1-related congenital fiber type disproportion. *Ann. Neurol.* **61**, 552–561 (2007).
46. K. Donner *et al.*, Mutations in the beta-tropomyosin (TPM2) gene—a rare cause of nemaline myopathy. *Neuromuscul. Disord.* **12**, 151–158 (2002).
47. O. E. Karpicheva, P. Robinson, A. Piers, Y. S. Borovikov, C. S. Redwood, The nemaline myopathy-causing E117K mutation in beta-tropomyosin reduces thin filament activation. *Arch. Biochem. Biophys.* **536**, 25–30 (2013).
48. C. M. Risi *et al.*, High-resolution cryo-EM structure of the junction region of the native cardiac thin filament in relaxed state. *PNAS Nexus* **2**, pgac298 (2023).
49. M. J. Greenberg, J. C. Tardiff, Complexity in genetic cardiomyopathies and new approaches for mechanism-based precision medicine. *J. Gen. Physiol.* **153**, e202012662 (2021).
50. K. Crawford *et al.*, Mice lacking skeletal muscle actin show reduced muscle strength and growth deficits and die during the neonatal period. *Mol. Cell Biol.* **22**, 5887–5896 (2002).
51. N. Sun *et al.*, Patient-specific induced pluripotent stem cells as a model for familial dilated cardiomyopathy. *Sci. Transl. Med.* **4**, 130ra147 (2012).
52. H. Wu *et al.*, Epigenetic regulation of phosphodiesterases 2A and 3A underlies compromised beta-adrenergic signaling in an iPSC model of dilated cardiomyopathy. *Cell Stem Cell* **17**, 89–100 (2015).
53. K. M. Broughton *et al.*, A myosin activator improves actin assembly and sarcomere function of human-induced pluripotent stem cell-derived cardiomyocytes with a troponin T point mutation. *Am. J. Physiol. Heart Circ. Physiol.* **311**, H107–H117 (2016).
54. K. C. Yang *et al.*, Novel adult-onset systolic cardiomyopathy due to MYH7 E848G mutation in patient-derived induced pluripotent stem cells. *JACC Basic Transl. Sci.* **3**, 728–740 (2018).
55. R. J. Zaunbrecher *et al.*, Cronos titin is expressed in human cardiomyocytes and necessary for normal sarcomere function. *Circulation* **140**, 1647–1660 (2019).
56. D. K. Ceholski *et al.*, Functional and transcriptomic insights into pathogenesis of R9C phospholamban mutation using human induced pluripotent stem cell-derived cardiomyocytes. *J. Mol. Cell Cardiol.* **119**, 147–154 (2018).
57. S. K. Barrick, L. Greenberg, M. J. Greenberg, A troponin T variant linked with pediatric dilated cardiomyopathy reduces the coupling of thin filament activation to myosin and calcium binding. *Mol. Biol. Cell* **32**, 1677–1689 (2021).
58. J. M. Winter *et al.*, Mutation-specific effects on thin filament length in thin filament myopathy. *Ann. Neurol.* **79**, 959–969 (2016).
59. C. T. Pappas, G. P. Farman, R. M. Mayfield, J. P. Konhilas, C. C. Gregorio, Cardiac-specific knockout of Lmod2 results in a severe reduction in myofilament force production and rapid cardiac failure. *J. Mol. Cell Cardiol.* **122**, 88–97 (2018).
60. C. T. Pappas *et al.*, Knockout of Lmod2 results in shorter thin filaments followed by dilated cardiomyopathy and juvenile lethality. *Proc. Natl. Acad. Sci. U.S.A.* **112**, 13573–13578 (2015).
61. V. M. Fowler, R. Dominguez, Tropomodulins and leiomodins: Actin pointed end caps and nucleators in muscles. *Biophys. J.* **112**, 1742–1760 (2017).
62. M. Boczkowska, Z. Yurtsever, G. Rebowski, M. J. Eck, R. Dominguez, Crystal structure of leiomodin 2 in complex with actin: A structural and functional reexamination. *Biophys. J.* **113**, 889–899 (2017).
63. Z. Wang *et al.*, Structures from intact myofibrils reveal mechanism of thin filament regulation through nebulin. *Science* **375**, eabn1934 (2022).
64. M. Janco *et al.*, Polymorphism in tropomyosin structure and function. *J. Muscle Res. Cell Motil.* **34**, 177–187 (2013).
65. S. Jansen, B. L. Goode, Tropomyosin isoforms differentially tune actin filament length and disassembly. *Mol. Biol. Cell* **30**, 671–679 (2019).
66. J. Huang *et al.*, CHARMM36m: An improved force field for folded and intrinsically disordered proteins. *Nat. Methods* **14**, 71–73 (2017).
67. R. B. Best *et al.*, Optimization of the additive CHARMM all-atom protein force field targeting improved sampling of the backbone  $\phi$ ,  $\psi$  and side-chain  $\chi_1$  and  $\chi_2$  dihedral angles. *J. Chem. Theory Comput.* **8**, 3257–3273 (2012).
68. N. Michaud-Agrawal, E. J. Denning, T. B. Woolf, O. Beckstein, MDAAnalysis: A toolkit for the analysis of molecular dynamics simulations. *J. Comput. Chem.* **32**, 2319–2327 (2011).
69. R. J. Gowers *et al.*, "MDAnalysis: A python package for the rapid analysis of molecular dynamics simulations" in *Proceedings of the 15th Python in Science Conference 2016 (SciPy 2016)*, S. Benthall, S. Rostrup, Eds. (Austin, TX, 2019), pp. 98–105.
70. K. K. Wen, X. Yao, P. A. Rubenstein, GTP-yeast actin. *J. Biol. Chem.* **277**, 41101–41109 (2002).
71. S. Jansen *et al.*, Single-molecule imaging of a three-component ordered actin disassembly mechanism. *Nat. Commun.* **6**, 7202 (2015).
72. S. M. Chin *et al.*, N-terminal acetylation and arginylation of actin determines the architecture and assembly rate of linear and branched actin networks. *J. Biol. Chem.* **298**, 102518 (2022).
73. T. D. Pollard, Measurement of rate constants for actin filament elongation in solution. *Anal. Biochem.* **134**, 406–412 (1983).
74. M. Gui, X. Wang, S. K. Dutcher, A. Brown, R. Zhang, Ciliary central apparatus structure reveals mechanisms of microtubule patterning. *Nat. Struct. Mol. Biol.* **29**, 483–492 (2022).
75. R. Zhang, G. M. Alushin, A. Brown, E. Nogales, Mechanistic origin of microtubule dynamic instability and its modulation by EB proteins. *Cell* **162**, 849–859 (2015).
76. A. Punjani, J. L. Rubinstein, D. J. Fleet, M. A. Brubaker, cryoSPARC: Algorithms for rapid unsupervised cryo-EM structure determination. *Nat. Methods* **14**, 290–296 (2017).
77. S. R. Clippinger *et al.*, Mechanical dysfunction of the sarcomere induced by a pathogenic mutation in troponin T drives cellular adaptation. *J. Gen. Physiol.* **153**, e202012787 (2021).
78. G. Pardon *et al.*, Insights into single hiPSC-derived cardiomyocyte phenotypes and maturation using ConTraX, an efficient pipeline for tracking contractile dynamics. *bioRxiv* [Preprint] (2021). <https://doi.org/10.1101/2021.03.18.436014> (Accessed 3 January 2024).
79. Y. Parasas *et al.*, CalTrack: High-throughput automated calcium transient analysis in cardiomyocytes. *Circ. Res.* **129**, 326–341 (2021).
80. A. Garg *et al.*, Data from "Dilated cardiomyopathy-associated skeletal muscle actin (ACTA1) mutation R256H disrupts actin structure and function and causes cardiomyocyte hypocontractility." Johns Hopkins Libraries. <https://doi.org/10.7281/T1/MX05CQ>. Deposited 15 October 2024.
81. A. Garg, M. J. Greenberg, R. Zhang, Cryo-EM structure of recombinant wildtype ACTA1 phalloidin-stabilized F-actin. Protein Data Bank. <https://www.rcsb.org/structure/9DUU>. Deposited 4 October 2024.
82. A. Garg, M. J. Greenberg, R. Zhang, Cryo-EM structure of recombinant wildtype ACTA1 phalloidin-stabilized F-actin. EMD. <https://www.ebi.ac.uk/emdb/EMD-47179>. Accessed 23 October 2024.
83. A. Garg, M. J. Greenberg, R. Zhang, Cryo-EM structure of recombinant R254H ACTA1 phalloidin-stabilized F-actin. PDB. <https://www.rcsb.org/structure/9DUV>. Deposited 4 October 2024.
84. A. Garg, M. J. Greenberg, R. Zhang, Cryo-EM structure of recombinant R254H ACTA1 phalloidin-stabilized F-actin. EMD. <https://www.ebi.ac.uk/emdb/EMD-47180>. Accessed 23 October 2024.